NANO LETTERS

2008
Vol. 8, No. 5
1404-1409

# Three-Dimensional Composition Profiles of Single Quantum Dots Determined by Scanning-Probe-Microscopy-Based Nanotomography

**Armando Rastelli,[*,†] Mathieu Stoffel,[†] Angelo Malachias,[‡,§] Tsvetelina Merdzhanova,[‡] Georgios Katsaros,[‡] Klaus Kern,[‡] Till H. Metzger,[§] and Oliver G. Schmidt[†]**

*Institute for Integrative Nanosciences, IFW Dresden, Helmholtzstrasse 20, D-01069 Dresden, Germany, Max-Planck-Institut für Festkörperforschung, Heisenbergstrasse 1, D-70569 Stuttgart, Germany, and European Synchrotron Radiation Facility, Boîte Postale 220, F-38043 Grenoble Cedex, France*

*Received January 29, 2008; Revised Manuscript Received March 11, 2008*

## ABSTRACT

**Scanning probe microscopy combined with selective wet chemical etching is employed to quantitatively determine the full three-dimensional (3D) composition profiles of single strained SiGe/Si(001) islands. The technique allows us to simultaneously obtain 3D profiles for both coherent and dislocated islands and to collect data with large statistics. Lateral and vertical composition gradients are observed, and their origin is discussed. X-ray scattering measurements performed on a large sample area are used to validate the results.**

Lattice-mismatched epitaxial growth of self-assembled quantum dots (QDs) keeps attracting much interest as it provides a straightforward route to the fabrication of defect-free nanostructures confining the motion of charge carriers in three-dimensions.[1] During growth, the deposited material mixes with the substrate material, leading to the formation of alloyed nanocrystals. Intermixing, a general phenomenon occurring for different material combinations, is driven by entropy of mixing[2] and leads to a reduction of misfit strain between epilayer and substrate. Since the electronic properties of QDs are ultimately determined by their atomistic structure or, in a continuum approximation, by their three-dimensional (3D) composition profile, the mechanisms leading to intermixing and their dependence on the growth conditions have been thoroughly studied in recent years, especially for the SiGe/Si model system.[2–14] The general picture emerging from these studies is that intermixing is mainly due to surface processes,[10,12] while bulklike intraisland diffusion may take place when surface diffusion is inhibited.[13]

The QD composition has been experimentally probed by various methods, such as anomalous X-ray scattering (AXS),[14–16] X-ray photoelectron microscopy,[7,17] Raman spectroscopy,[8] cross-sectional transmission electron microscopy (TEM) combined with electron energy loss spectroscopy,[18,19] and cross-sectional scanning tunneling microscopy,[20] and by analyzing the deformation induced by buried QDs on the surface of the capping layer.[21] Some of these techniques can access the composition by averaging over a statistical ensemble of QDs (or islands), thus neglecting possible island-to-island variations.[16,14,8,22] Others are limited to cross sectional profiles[18–20] or only to the surface composition.[7,17] Electron tomography using Z-contrast imaging in scanning TEM[23,24] is a promising approach to obtain composition maps of single QDs, but the method has not provided absolute composition values so far. Selective wet chemical etching combined with atomic force microscopy (AFM) has emerged as a simple tool to gather information on the local composition of SiGe layers and single QDs,[4,6,11,13,16,25,26] but also in this case no routes to obtain *quantitative* 3D composition profiles have been proposed.

In this work we show that multistep selective wet chemical etching, AFM imaging of the same areas, and dedicated reconstruction algorithms can be exploited to determine the *quantitative* 3D composition profiles of individual QDs and gather statistically significant information to correlate the island composition with its morphology. Apart from the reconstruction procedure and the considered material system, the technique is similar to the "nanotomography" employed

* Corresponding author. E-mail: a.rastelli@ifw-dresden.de. Phone: +49 (0)351 4659 659. Fax: +49 (0)351 4659 782.
† Institute for Integrative Nanosciences, IFW Dresden.
‡ Max-Planck-Institut für Festkörperforschung.
§ European Synchrotron Radiation Facility.

10.1021/nl080290y CCC: $40.75 © 2008 American Chemical Society
**Published on Web 04/01/2008**

by Magerle[27] to reveal the 3D shape of buried nanostructures. With the nanotomography approach we observe that the Ge content drops from the top to the base of the islands independently of their shape. For coherent islands, slightly asymmetric profiles are observed which correlate with the occurrence of shallow facets. Moreover, the average Ge fraction monotonically increases moving from small and shallow coherent islands to large and plastically relaxed islands.

The sample studied here was grown by solid-source molecular beam epitaxy (MBE) on a Si(001) substrate. After Si buffer growth, 15 monolayers (ML) of Ge were deposited at a substrate temperature of 740 °C and at a rate of 0.04 ML/s. With such parameters we obtain significantly alloyed islands with different shapes. The sample was cooled to room temperature (RT) immediately after growth for etching and imaging with a commercial open-loop AFM operated in tapping mode. Particular care was taken in choosing tips and scanning parameters to limit scanning artifacts. The selective wet chemical etching was performed at RT with a NHH solution [1:1 vol. (28% $NH_4OH$):(31% $H_2O_2$)], which shows an etching rate $r$ increasing approximately exponentially with the Ge fraction $x$,[11,28] no preferential etching direction, and a negligible dependence on the strain of the SiGe material[28] (see below). Before each etching step, the sample was dipped in a diluted HF solution to remove the surface oxide and a fresh NHH solution was prepared. The same sample area was located after different etching times $t_i$ = 0, 6, 18, 30, 40, 50, 60, 80, 100, 120, 140, 160, 180, 240, 260, 290 min. The reliability of the composition values obtained by nanotomography was tested by performing AXS measurements on the same sample in grazing-incidence at the ID01 beamline of the European Synchrotron Radiation Facility. Longitudinal ($\theta-2\theta$) scans were measured in the vicinity of the Si(400) reflection for two selected energies: (i) 11103 eV (Ge K-edge) and (ii) 60 eV below (i). Since for these two energies, close to the K-edge of Ge, only the atomic scattering factor of Ge changes, the contrast observed in the diffracted intensity can be used to infer quantitatively the amount of Ge inside the islands.[14,16]

Figure 1a shows a representative AFM image of the sample surface prior to etching ($t_0$ = 0). Most of the islands are coherent domes (Ds) and islands with intermediate shape between domes and steeper barns (TBs). Large and small plastically relaxed superdomes (SD and SSD, respectively) are also observed because of the large amount of deposited Ge. A few transition islands (TDs) with intermediate morphology between shallow {105} faceted pyramids and Ds are observed in larger scale images (see insets in panels b and c of Figure 3). Islands are surrounded by trenches which penetrate into the Si substrate[3,29] and are well visible at any etching step. By using the centers of such trenches as control points, we aligned the images to the image taken at $t_0$ = 0. (Interpolation was applied to compensate nonlinearities of the AFM scanner). Panels b−f of Figure 1 show some of the resulting images taken at increasing $t$. While the surface is smooth prior to etching (Figure 1a) and after complete removal of the SiGe material (Figure 1f), the

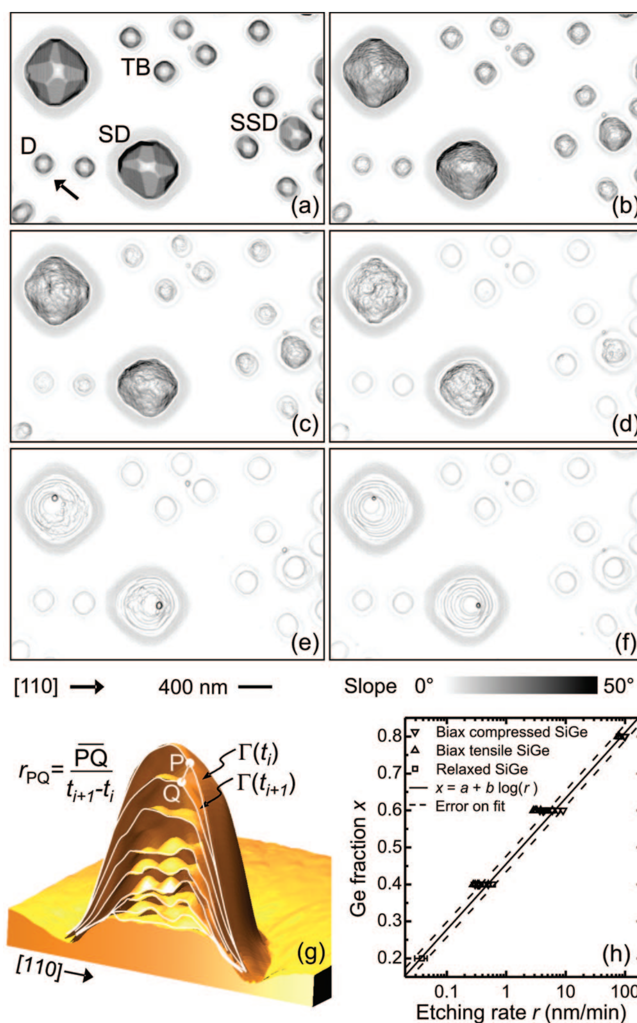


**Figure 1.** (a−f) Sequence of AFM images of the same surface area of a sample obtained by depositing 15 ML of Ge on Si(001) at 740 °C and selectively etched in NHH solution for 0 (a), 40 (b), 80 (c), 140 (d), 240 (e), and 290 min (f). (g) 3D view of a cross-cut through the island marked in (a) etched and measured 15 times and schematic illustration of the definition of local etching rate $r$. The image scale is 400 × 245 × 26 $nm^3$. (h) Etching rate calibration data displayed as Ge fraction $x$ as a function of etching rate $r$. Data points were determined from the etching of SiGe layers with different strain. The result of the fit and the corresponding errors are shown as solid and dashed lines, respectively.

surface of partially etched islands shows some random "bumps", which we attribute to etching-induced roughening. In fact, by averaging a few profiles of islands with similar initial size and morphology, smooth surfaces are restored at different $t_i$ (not shown). From line scans of the AFM images (see Figure 1g and Figure 2d−g) we observe that the amplitude of the roughness is about 2–3 nm. Such roughness, together with the finite size of the AFM tip, limits at present the spatial resolution achievable with the method. We will therefore limit our discussion to features larger than the observed roughness.

In order to reconstruct the local etching rate in 3D, for each point **P** belonging to the surface $\Gamma(t_i)$ measured at $t_i$, we determine the nearest point $\mathbf{Q} \in \Gamma(t_{i+1})$ (see Figure 1g). Assuming that **P** evolves into **Q** during etching, we can assign to the points **S** on the segment **PQ** a local etching

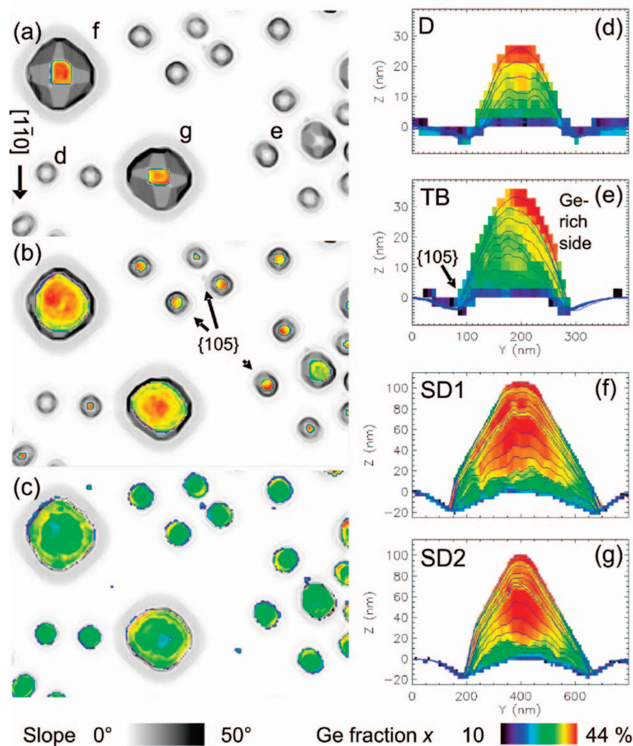


**Figure 2.** (a−c) Horizontal cross-cuts of the islands shown in Figure 1a with color-coded in-plane composition at heights $z$ = 86 (a), 26 (b), and 2 nm (c) with respect to the substrate level. (d−g) Vertical cross-cuts of the islands marked in (a) taken along the [1$\bar{1}$0] ($y$) direction. The curves on top of the composition maps represent line scans of the surfaces $\Gamma(t_i)$ measured at different etching times $t_i$.

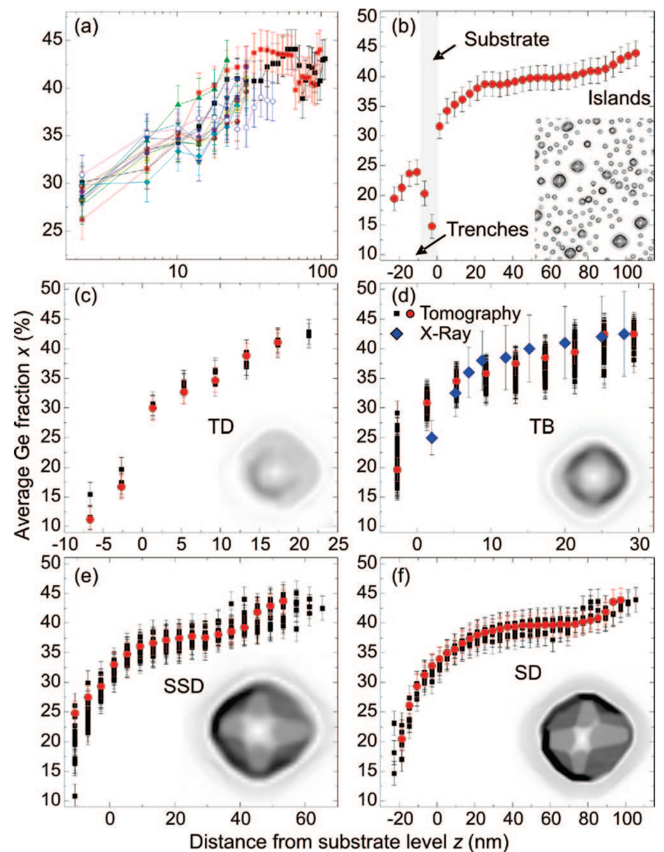


**Figure 3.** (a) Ge fraction $x$ for the islands shown in Figure 1 along a line parallel to the growth direction ($z$) and passing though the center of the island base. (b) Average $x$ for the area shown in the inset (scale 4.4 × 5.2 $\mu$m$^2$) as a function of distance from the substrate level ($z$ = 0). Regions corresponding to trenches, substrate, and islands are indicated. (c−f) Average $x$ as a function of $z$ for different island types: (c) TDs; (d) Ds and TBs; (e) SSDs; (f) SDs. The data points marked in red in (c−f) correspond to the islands shown in the respective insets, with scale 300 × 300 × 20 nm$^3$ (c), 300 × 300 × 32 nm$^3$ (d), 400 × 400 × 53 nm$^3$ (e), and 700 × 700 × 101 nm$^3$ (f). In (d) the values obtained from AXS are reported for comparison.

rate $r_{\mathbf{PQ}} = \overline{\mathbf{PQ}}/(t_{i+1} - t_i)$. The relation between Ge fraction $x$ and $r$ is shown in Figure 1h, where the data points represent $r$ values determined on $Si_{1-x}Ge_x$ layers grown on strain-relaxed $Si_{1-y}Ge_y$ buffers.[28] Relaxed layers have $x = y$, while layers under biaxial compressive and tensile stress have $x = y + 0.2$ and $x = y - 0.2$, respectively. While $r$ strongly depends on $x$, no systematic dependence on the strain state was detected within the measurement uncertainties.[28] To obtain an analytic relation between $x$ and $r$, we fitted the data with a phenomenological function $x = a + b \log(r)$. For a given composition, we assume a (conservative) error bar on the $r$ ranging from the minimum to the maximum rate values for that particular composition. The result of the fit and the corresponding error are shown as continuous and dashed lines in Figure 1h. To display the local composition, we construct a 3D matrix, with each voxel (bin or pixel in 3D) $\Omega_{ijk}$ being assigned a value $x_{ijk} = a + b \log(r_{ijk})$, where $r_{ijk}$ is the mean etching rate for the irregularly gridded points $\mathbf{S} \in \Omega_{ijk}$. The choice of the voxel size is rather arbitrary, and different choices were found to produce similar results. In order to limit and average out spurious effects due to the surface roughness during etching, a lateral size given by twice the size of the pixels of the original AFM images was assumed, while the vertical resolution was fixed to 4 nm (larger than the roughness amplitude).

Panels a−c of Figure 2 show cross-cuts of the image shown in Figure 1a perpendicular to the growth ($z$) direction and taken at decreasing $z$ distance from the substrate level (at $z$ = 0 nm). The values of $x_{ijk}$ are color-coded. Both for coherent and dislocated islands, the Ge fraction drops moving from the island top toward the substrate. This finding (see also the cross-cuts parallel to $z$ in Figure 2d−g) is consistent with data previously obtained by other methods on the SiGe system[16,18,19,30] and also on other material systems.[22] Moreover, the Ge fraction through the island axes has absolute values which depend on $z$ but not on the particular island size and shape (with the exception of SSDs, which will be discussed later). In particular, the regions of the islands with small $z$, uncovered at different etching times depending on the initial island size, have similar $x$, as illustrated in Figure 3a. For most of the coherent islands we also observe a slight lateral asymmetry in the composition (see Figure 2b,e), which correlates with a slight morphological asymmetry, i.e. the "Ge rich" side close to the island top invariably appears on the opposite side with respect to shallow {105} facets at the island base. This asymmetry would be washed out in ensemble measurements, such as those obtained by AXS.

SDs (see Figure 2f,g) show a Ge-rich core surrounded by a Si-richer shell close to the island base.

In order to probe a statistically significant number of islands, we considered a larger scale area (see inset of Figure 3b). Apart from a larger voxel size, the 3D composition matrix is computed as for the images shown in Figure 1. The vertical gradient of the Ge fraction in the film is shown in Figure 3b, where $x$ is averaged over matrix planes with constant $z$. The data points at $z < 0$ correspond to Si-rich SiGe material inside the trenches. The drop in $x$ observed close to $z = 0$ is an artifact of the measurement due to a nonperfect overlap of the images, and consequent random fluctuations of the extracted composition. This problem is solved by excluding the substrate from the analysis (Figure 3c−f). For $0 \lesssim z \lesssim 25$ nm we observe a relatively steep increase of $x$, which is attributed to the steep increase in $x$ for both coherent islands and large SDs. The smoother increase for $z \gtrsim 25$ nm is ascribed to the rather homogeneous composition of the upper portion of SDs. This interpretation is supported by the vertical composition profiles for islands with different size/morphology observed in the image shown in the inset of Figure 3b. Small TDs (Figure 3c) show an almost linear increase of $x$ with $z$. Steep coherent islands (Ds and TBs, Figure 3d) show a continuous but sublinear increase of $x$ with $z$. Small (Figure 3e) and large (Figure 3f) dislocated islands show a plateau in the value of $x$ above a certain value of $z$. To corroborate the above results, the Ge concentration $x$ was also extracted for Ds and TBs from grazing-incidence AXS measurements. Following the procedure of the iso-strain scattering method[22] the local in-plane lattice parameter and $x$ extracted from the longitudinal scans can be directly related to real space positions inside islands by matching the lateral size information obtained by transversal ($\theta$) scans in X-ray with typical AFM profiles (for a detailed discussion see ref 15). As a result, the vertical concentration profile $x$, which corresponds to the average of the lateral SiGe content, can be expressed as a function of $z$ and used for a direct comparison with the results of this work. For Ds and TBs, the AXS result is represented by the diamond dots in Figure 3d and exhibit a very good agreement with the values obtained by the AFM nanotomography. On the other hand the X-ray method for extracting the lateral Ge composition profile described in ref 16 could not be used here. Since it relies on the correct fitting of X-ray form factor and lateral composition, its application is in fact limited to monodisperse ensembles of islands with narrow size distribution. Finally, the ability of the AXS method to produce a height-dependent concentration profile lies in the inherent monotonic strain relaxation (from the bottom to the apex) of coherent uncapped islands. Since this is not the case for dislocated superdomes, only an average Ge fraction of 47 ± 6% is determined by AXS for the relaxed material in these islands (for $z \gtrsim 30$ nm), in agreement with the findings of this work.

By averaging $x$ over all the matrix voxels belonging to a given island, we can extract its average composition $\bar{x}$ and correlate it to the island size and surface morphology. Since the last image taken during the etching sequence (at $t_f$ = 290 min) contains information on the Si substrate profile, we subtract the substrate level from the image collected at $t_0 = 0$ and thus obtain the volume $V_{SiGe}$ of only the SiGe material composing the islands. In Figure 4a we observe that $\bar{x}$ increases with island size, moving from ~28% for small and shallow islands to ~35% for dislocated islands. Such an increase can be rationalized by the fact that both steep and dislocated islands are less strained than shallow islands and thus represent more favorable locations for the accumulation of Ge. On the other hand, larger islands exert an increasing stress on the Si substrate, promoting the formation of wider and deeper trenches at their foot. The Si expelled from the trenches can climb the surface of the growing islands (as suggested by the Si-rich shells seen in Figure 2f,g), thus partially compensating the Ge enrichment.[6] By evaluating the volume of Si removed from the trench below and surrounding each island $V_{trench}$, we can quantify the impact of this Si source on the island composition. By plotting the ratio $V^*_{trench} = V_{trench}/[V_{SiGe}(1 - \bar{x})]$ as a function of island volume $V_{SiGe}$ (inset of Figure 4a), we see that trenches provide about 40% of the Si contained into coherent (TDs, Ds, TBs) and small dislocated islands (SSDs) and up to about 65% of the Si contained in the large superdomes (SDs). The remaining Si must therefore originate from other areas of the substrate through long-range diffusion.[10,11,29] We can directly correlate $\bar{x}$ with the surface morphology by computing the fraction of the island surface occupied by {105} facet (Figure 4b). The total surface area and the area occupied by {105} facets are easily calculated from the AFM image taken at $t_0$.[31,32] As expected from Figure 4a, the Ge fraction decreases monotonically with increasing {105} facet area.

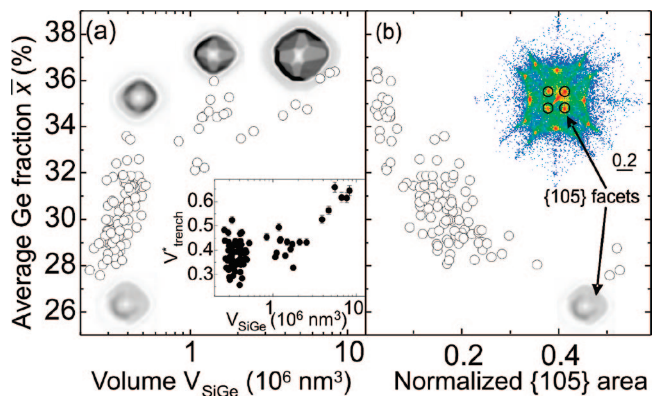


**Figure 4.** (a) Average Ge fraction $\bar{x}$ and Si fraction originating from the trenches $V^*_{trench}$ (inset) for the islands shown in Figure 3b as a function of island volume $V_{SiGe}$. (b) $\bar{x}$ as a function of normalized {105} facet area showing the correlation between surface morphology and composition. The inset displays the "facet plot"[31] for all islands on the sample, with each spot corresponding to a different facet. The error bars on $\bar{x}$ are of about ±2%. The scale of the AFM images included in (a) is the same as that in Figure 3.

We now discuss the origin of the observed composition profiles. At the early stages of Ge growth, an alloyed wetting layer (WL) is formed. Beyond a critical thickness of ~4 ML shallow islands appear and evolve into {105} faceted pyramids. Besides the deposited Ge, part of the WL is

consumed by such islands,[33,34] which then further evolve into steeper Ds and then Bs through material accumulation at their surface.[35] Since under our experimental conditions intermixing takes place through surface diffusion,[6,12,13] the observation of a Si-rich island base common to all islands (see Figure 3a) suggests that the initial pyramids are Si-rich, possibly because of the substantial contribution of the WL to their growth. At a Ge coverage of ~10 ML, all coherent islands have reached a steep B morphology.[31] Further deposition leads to the appearance of dislocations in some of the Bs growing beyond the critical size.[36] Because of the strain relaxation provided by dislocations, most of the subsequently deposited Ge (~5 ML) is incorporated into such SDs,[31] which efficiently grow in a cyclic fashion with increasing number of dislocations. (From the number of "rings" seen at $t_f$, we estimate that the SDs observed here contain up to 11–12 dislocations[37]). In the absence of an effective Ge flux, the time needed for the deposition of 5 ML Ge (about 2 min), is roughly equivalent to an annealing step for most of the coherent islands (Bs). During this "annealing" step, the strain in the film can be released by two mechanisms: (i) ripening of SDs at the expense of Bs, and (ii) surface-mediated intermixing of Bs. Process (i) leads to a volume reduction of Bs and consequent shape change to TB, D, and TD and allows us to explain the presence of shallow islands on the surface. Process (ii), which usually takes place in an asymmetric fashion,[10,11] allows us to explain the slightly asymmetric composition profiles observed in Figure 2b,e, the occurrence of {105} facets at the island base, and the reduction of aspect ratio compared to the Bs observed in the film at 10 ML of Ge deposition.[31] On the other hand, since the Ge flux is not interrupted, some of the coherent islands close to the critical size can still introduce dislocations after having further intermixed by lateral motion.[10,11] SSDs, with up to two dislocations, probably originate from this process, as indicated by the asymmetry of the Si plateau below them (Figure 1a,f) and by the difference in composition profile compared to SDs (Figure 3e,f).

In conclusion, we have presented a novel method to quantitatively determine the full 3D composition profiles of self-assembled QDs. Vertical and lateral composition gradients were observed, correlated to the island morphology, and their origin was discussed. Compared to existing techniques, such as AXS and TEM, the present method relies on the use of simple experimental equipment and offers all advantages of scanning probe microscopy, such as high spatial resolution and the capability of measuring relatively large sample areas to obtain information both on single nano-objects and on average properties. On the other hand, since the reconstruction of the local composition relies on the surface imaging of progressively etched islands, the method cannot be applied in situations where underetching may take place (very Si rich layer on top of almost pure Ge). The spatial resolution may be possibly improved by seeking for etching conditions which minimize etching-induced roughening, by using ultrasharp AFM tips and by performing a larger number of etching steps with small time intervals. Furthermore, the use of a closed-loop scanner would limit lateral and vertical distortions of the AFM images and facilitate the registering procedure. Finally, detailed simulations of the etching process for different starting morphologies and composition profiles may help in optimizing the reconstruction algorithms. Subject to availability of proper etchants, the technique could be applied to other material systems and nanostructures other than QDs.

**Acknowledgment.** The authors acknowledge M. S. Leite, G. Medeiros-Ribeiro, L. Miglio, F. Montalenti, G. Bauer, and J. Tersoff for fruitful discussions. This work was supported by the BMBF (No. 03N8711) and the EU project D-DotFET (No. 012150).

## References

(1) *Single Quantum Dots: Fundamentals, Applications and New Concepts*; Michler, P., Ed.; Springer: Berlin, 2003.
(2) Medeiros-Ribeiro, G.; Stanley Williams, R. *Nano Lett.* **2007**, *7* (2), 223–226.
(3) Kamins, T. I.; Medeiros-Ribeiro, G.; Ohlberg, D. A. A.; Stanley Williams, R. *J. Appl. Phys.* **1999**, *85* (2), 1159–1171.
(4) Schmidt, O. G.; Denker, U.; Christiansen, S.; Ernst, F. *Appl. Phys. Lett.* **2002**, *81* (14), 2614–2616.
(5) De Seta, M.; Capellini, G.; Evangelisti, F.; Spinella, C. *J. Appl. Phys.* **2002**, *92* (1), 614–619.
(6) Denker, U.; Stoffel, M.; Schmidt, O. G. *Phys. Rev. Lett.* **2003**, *90* (19), 196102.
(7) Ratto, F.; Rosei, F.; Locatelli, A.; Cherifi, S.; Fontana, S.; Heun, S.; Szkutnik, P.-D.; Sgarlata, A.; de Crescenzi, M.; Motta, N. *J. Appl. Phys.* **2005**, *97* (4), 043516.
(8) Milekhin, A. G.; Nikiforov, A. I.; Ladanov, M. Y.; Pchelyakov, O. P.; Lobanov, D. N.; Novikov, A. V.; Krasil'Nik, Z. F.; Schulze, S.; Zahn, D. R. T. *Physica E* **2004**, *21* (2–4), 464–468.
(9) Hadjisavvas, G.; Kelires, P. C. *Phys. Rev. B* **2005**, *72* (7), 075334.
(10) Denker, U.; Rastelli, A.; Stoffel, M.; Tersoff, J.; Katsaros, G.; Costantini, G.; Kern, K.; Jin-Phillipp, N. Y.; Jesson, D. E.; Schmidt, O. G. *Phys. Rev. Lett.* **2005**, *94* (21), 216103.
(11) Katsaros, G.; Rastelli, A.; Stoffel, M.; Isella, G.; von Känel, H.; Bittner, A. M.; Tersoff, J.; Denker, U.; Schmidt, O. G.; Costantini, G.; Kern, K. *Surf. Sci.* **2006**, *600* (12), 2608–2613.
(12) Tu, Y.; Tersoff, J. *Phys. Rev. Lett.* **2007**, *98* (9), 096103.
(13) Leite, M. S.; Medeiros-Ribeiro, G.; Kamins, T. I.; Stanley Williams, R. *Phys. Rev. Lett.* **2007**, *98* (16), 165901.
(14) Schülli, T. U.; Stoffel, M.; Hesse, A.; Stangl, J.; Lechner, R. T.; Wintersberger, E.; Sztucki, M.; Metzger, T. H.; Schmidt, O. G.; Bauer, G. *Phys. Rev. B* **2005**, *71* (3), 035326.
(15) Magalhães-Paniago, R.; Medeiros-Ribeiro, G.; Malachias, A.; Kycia, S.; Kamins, T. I.; Stanley Williams, R. *Phys. Rev. B* **2002**, *66* (24), 245312.
(16) Malachias, A.; Kycia, S.; Medeiros-Ribeiro, G.; Magalhães-Paniago, R.; Kamins, T. I.; Stanley Williams, R. *Phys. Rev. Lett.* **2003**, *91* (17), 176101.
(17) Biasiol, G.; Heun, S.; Golinelli, G. B.; Locatelli, A.; Mentes, T. O.; Guo, F. Z.; Hofer, C.; Teichert, C.; Sorba, L. *Appl. Phys. Lett.* **2005**, *87* (22), 223106.
(18) Floyd, M.; Zhang, Y.; Driver, K. P.; Drucker, J.; Crozier, P. A.; Smith, D. J. *Appl. Phys. Lett.* **2003**, *82* (9), 1473–1475.
(19) Schade, M.; Heyroth, F.; Syrowatka, F.; Leipner, H. S.; Boeck, T.; Hanke, M. *Appl. Phys. Lett.* **2007**, *90* (26), 263101.
(20) Offermans, P.; Koenraad, P. M.; Wolter, J. H.; Pierz, K.; Roy, M.; Maksym, P. A. *Phys. Rev. B* **2005**, *72* (16), 165332.
(21) Springholz, G.; Abtin, L.; Holý, V. *Appl. Phys. Lett.* **2007**, *90* (11), 113119.
(22) Kegel, I.; Metzger, T. H.; Lorke, A.; Peisl, J.; Stangl, J.; Bauer, G.; Nordlund, K.; Schoenfeld, W. V.; Petroff, P. M. *Phys. Rev. B* **2001**, *63* (3), 035318.
(23) Arslan, I.; Yates, T. J. V.; Browning, N. D.; Midgley, P. A. *Science* **2005**, *309* (5744), 2195–2198.
(24) Inoue, T.; Kita, T.; Wada, O.; Konno, M.; Yaguchi, T.; Kamino, T *Appl. Phys. Lett.* **2008**, *92* (3), 031902.
(25) Li, F. H.; Fan, Y. L.; Yang, X. J.; Jiang, Z. M.; Wu, Y. Q.; Zou, J. *Appl. Phys. Lett.* **2006**, *89* (10), 103108.
(26) Wu, C.-C.; Hull, R. *J. Appl. Phys.* **2006**, *100* (8), 083510.

(27) Magerle, R. *Phys. Rev. Lett.* **2000**, *85* (13), 2749–2752.
(28) Stoffel, M.; Malachias, A.; Merdzhanova, T.; Cavallo, F.; Isella, G.; Chrastina, D.; von Känel, H.; Rastelli, A.; Schmidt, O. G. arXiv: 0801.4211v1.
(29) Denker, U.; Schmidt, O. G.; Jin-Philipp, N.-Y.; Eberl, K. *Appl. Phys. Lett.* **2001**, *78* (23), 3723–3725.
(30) Schülli, T. U.; Stangl, J.; Zhong, Z.; Lechner, R. T.; Sztucki, M.; Metzger, T. H.; Bauer, G. *Phys. Rev. Lett.* **2003**, *90* (6), 066105.
(31) Stoffel, M.; Rastelli, A.; Tersoff, J.; Merdzhanova, T.; Schmidt, O. G. *Phys. Rev. B* **2006**, *74* (15), 155326.
(32) The image correction, alignment, tomography computation, and visualization were obtained by a software package based on the ITT-IDL Platform. The source can be downloaded at http://www.ifw-dresden.de/institutes/iin/members/ar5.
(33) Schmidt, O. G.; Lange, C.; Eberl, K *Appl. Phys. Lett.* **1999**, *75* (13), 1905–1907.
(34) Schülli, T. U.; Richard, M.-I.; Renaud, G.; Favre-Nicolin, V.; Wintersberger, E.; Bauer, G. *Appl. Phys. Lett.* **2006**, *89* (14), 162105.
(35) Montalenti, F.; Raiteri, P.; Migas, D. B.; von Känel, H.; Rastelli, A.; Manzano, C.; Costantini, G.; Denker, U.; Schmidt, O. G.; Kern, K.; Miglio, L. *Phys. Rev. Lett.* **2004**, *93* (21), 216102.
(36) Marzegalli, A.; Zinovyev, V. A.; Montalenti, F.; Rastelli, A.; Stoffel, M.; Merdzhanova, T.; Schmidt, O. G.; Miglio, L. *Phys. Rev. Lett.* **2007**, *99* (23), 235505.
(37) Merdzhanova, T.; Kiravittaya, S.; Rastelli, A.; Stoffel, M.; Denker, U.; Schmidt, O. G. *Phys. Rev. Lett.* **2006**, *96* (22), 226103.

NL080290Y